Hard Horn Design for Quasi-Optical Power Combining Using Solid-State Power Amplifiers

W. S. Pickens,[1] L. W. Epp,[1] and D. J. Hoppe[1]

In recent years, there has been significant interest in the use of corrugated, periodic structures to control the wave impedance of a given surface. It has been shown [1] that a quasi-transverse-electromagnetic (TEM) wave can be excited in a waveguide by correctly choosing the impedance at the guide wall. This correctly chosen impedance is referred to as the hard boundary condition. We have taken advantage of this property of the so-called "hard" guide to attempt to create a spatial power combiner/splitter that couples to an array of microstrip patch antennas feeding a bank of monolithic microwave integrated circuit (MMIC) power amplifiers. The hard horn described here employs longitudinal corrugations filled with a low-loss dielectric material along the vertical walls to achieve the hard boundary condition. We believe the use of dielectric-filled corrugations will improve the insertion loss performance over that of a hard guide using dielectric slabs bonded to the guide wall. Additionally, the horn is tapered to its maximum aperture along a cosine curve in order to improve return loss performance. Included in this article is a discussion of the fabrication process of prototype hard horns, measurements of a hard horn prototype, and preliminary modal analysis results.

I. Introduction and Background

In the mid-1980s, the concept of using quasi-optical (Q/O) power combining of solid-state sources became the subject of more intensive research by Mink [2] at the U.S. Army Research Office, among others. In fact, by 1983 quasi-optical power combining had been recognized (see Chang [3]) as a separate area of power combining. Since that time, significant theoretical development and technology demonstration efforts have taken place at the Jet Propulsion Laboratory (JPL) and elsewhere. More recently, Rutledge and others at the California Institute of Technology [4] and JPL have looked at quasi-optical power combining for high-power applications.

The basic concept of the solid-state power amplifier (SSPA) using Q/O power combining, as applied here, is to use a hard horn to achieve a transverse-electromagnetic (TEM) or plane-wave excitation in an aperture, which is filled with an antenna array. The goal of creating the TEM or plane-wave excitation

[1] Communications Ground Systems Section.

The research described in this publication was carried out by the Jet Propulsion Laboratory, California Institute of Technology, under a contract with the National Aeronautics and Space Administration.

is to produce an equal power distribution in the receiving antennas, so that the combination of the hard horn and antenna array creates a 1 to $(N \times N)$ power divider, where N is the number of antennas in a row or column of the square array. The antenna array then is connected via a very simple feed network to a number of high-efficiency monolithic microwave integrated circuit (MMIC) amplifiers, eliminating the need for lossy power combining structures in the feed network. These MMICs amplify the signals that are recombined via a hard horn. The result is a high-power, high-gain, millimeter-wave amplifier constructed using solid-state devices. The portion of this challenging undertaking described in this article is the analysis, design, and testing of a hard horn to provide a uniform, plane-wave-like illumination to the antenna array.

Work on an initial prototype began in September of 1998. The axial cross section of this prototype is shown in Fig. 1. This design was based on the approximate analysis of Kildal [5], which limited the prototype to a relatively small aperture. By keeping the aperture small, the approach attempted to minimize the effect of the excitation of higher-order modes. The evaluation of higher-order modes must be considered at every cross section of the waveguide, including the junctions that are necessary in the practical application of the device to the antenna array. For example, a junction is created by tapering into the dielectric that is used to create the hard boundary condition, as shown in section 2 in Fig. 1. In addition, tapering is created in any flaring section where the horn is dimensionally adjusted to match the size of the antenna array, so such a tapered section usually is found in section 3, where the corrugation depth remains constant as the waveguide dimensions increase.

Whereas section 2 in Fig. 1 represents a linear transition into the hard boundary condition, even when done in this first-order smooth manner, it represents many waveguide cross sections of various corrugation depths and modal representations [6]. Thus, it becomes impossible to view the hard horn design as simply a waveguide with one depth of corrugation. The need for the development of analytical techniques for the evaluation of a complete modal set of longitudinally corrugated waveguides becomes evident.

Although section 3 in Fig. 1 is shown as a straight section, there is a desire to create a large aperture to maximize the aperture efficiency of the horn [6]. Better aperture efficiency occurs with a larger aperture because of the existence of the fields in the dielectric filling the corrugations of the antenna. In the dielectric, the fields are tapered from the aperture [5]. By maximizing the ratio of aperture size to corrugation depth area, the power in the corrugations is minimized [6]. This goal, and the desire to create larger-sized arrays under the aperture to increase total output power, causes designers to look for tapered horns.

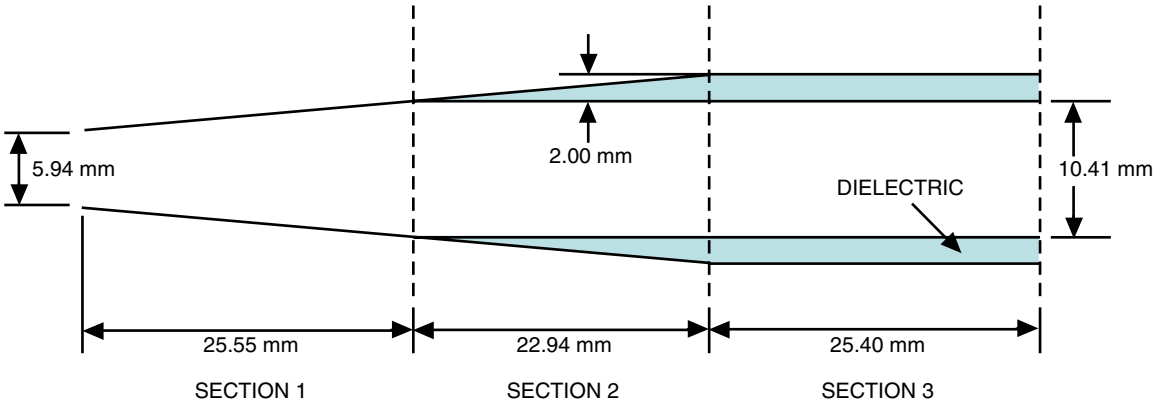

Fig. 1. Axial cross sections of a waveguide transition into a longitudinally corrugated waveguide.

The prototype, as depicted in the diagram of Fig. 1 and the photograph in Fig. 2(a), had all four walls corrugated. This prototype was intended for use in a dual-linear polarization system consisting of a quasi-optical amplifier working in reflection mode. The reflective grid amplifier tested with this horn in March of 1999 is shown at the bottom left of Fig. 2(a).

The horn design for the Q/O SSPA currently under development at JPL features longitudinally corrugated horizontal walls and a cosine taper from the original guide to the final aperture dimension, as shown in Fig. 2(b). The new design splits the power combining and re-combining tasks between two horns, and thereby eliminates the need for dual-linear operation and four corrugated walls. This simplifies the manufacturing and design of the horn. The current design uses a single-linear polarization and as such requires only the two walls parallel to the major electric field (E-field) component be corrugated; see Fig. 2(b).

Some preliminary results are presented and discussed in the context of the continuing development of the mode-matching code. This analytical work is motivated by measured data from the first hard horn prototype developed at JPL, shown in Fig. 2(a). This article concludes with a summary of completed and ongoing work. The goals for this task are lofty but potentially achievable. A successful demonstration of the SSPA system using the hard horn will represent a significant advance in the state of the art of spacecraft communications by creating an alternative to traveling-wave tube amplifiers (TWTAs) in spacecraft applications.

II. Measurement of a Dual-Linear Polarized Hard Horn

In this section, the near-field and network analyzer measurements of the prototype hard horn are discussed. The first measurements were the measurements of the scattering parameters (S-parameters) of the horn shown in Fig. 2(a). Define port 1 to represent a y-polarized wave at the 5.9436-mm aperture of section 1 in Fig. 1, and port 2 to represent the orthogonal x-polarized wave. Experimentally, this meant the attachment of an orthomode to the square rectangular aperture, so that these ports were measurable. Port 1 and port 2 are the inputs to a square rectangular waveguide, with metal perfect electric conductor (PEC) walls. Define port 3 to be the 10.414-mm aperture, as defined in section 3 in Fig. 1, which is surrounded by four corrugated walls.

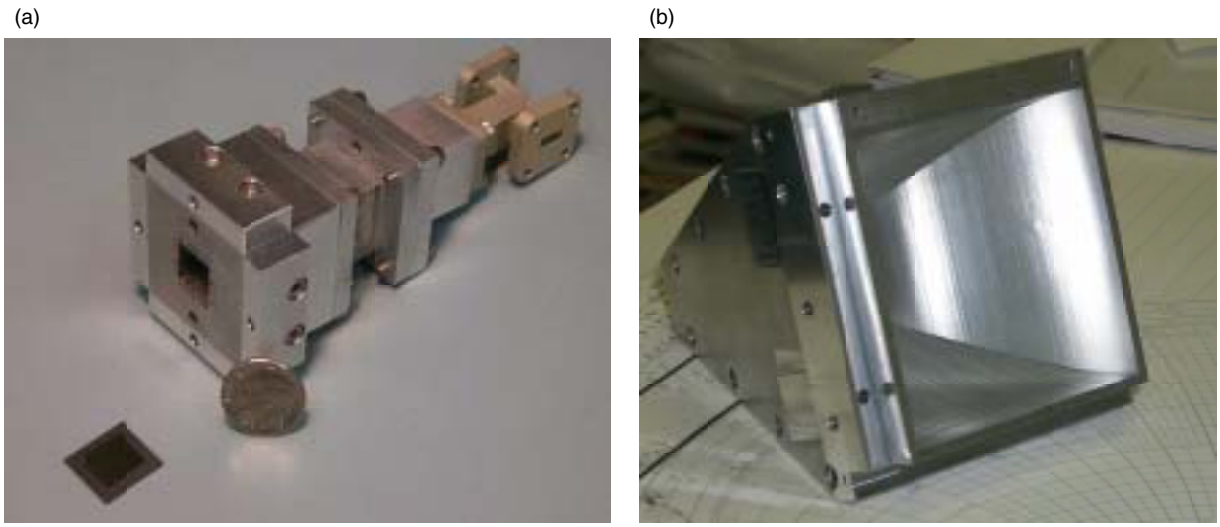

Fig. 2. Hard horn for (a) dual-linear polarization and (b) single-linear polarization.

Figure 3 shows the measurements when port 3 is allowed to radiate into free space. They show the return loss at port 1 and port 2 as S11 and S22, respectively. The coupling between these ports is measured as S12 and S21; these show the non-perfect isolation between ports of the orthomode used in the measurements. Note that the input match degrades at 32.3 GHz and also the slight variation between S11 and S22. Since the corrugations on all four walls are designed to be equal, this latter discrepancy is unexpected. Possible explanations include that the manufacturing tolerance of the Teflon-like dielectric material had a tolerance that exceeded the machined corrugation tolerance. This led to difficulty in consistently inserting the dielectric material into the corrugations, which were press fit. It also caused a distortion of the fins as the material was progressively placed in the corrugations, squeezing the material as the insertion continued along a wall. In addition, the dielectric material was observed to have ragged edges and fibers extending into the open waveguide.

Figure 4 shows the measured S-parameters at ports 1 and 2 when the aperture of the horn (port 3) was shorted against a metallic plate. This provides a measurement of twice the insertion loss down the horn, which shows a marked increase for frequencies greater than 32.1 GHz. For a PEC square waveguide with $a = 10.414$ mm, 32.2 GHz is the cut-off frequency for the transverse electric (TE)12 mode. An undesirable cross section for the existence of this mode exists in the transition from section 1 to section 2, where the hard boundary condition is being created. This originally was to be avoided. When the antenna array to be placed in the aperture was grown from 9.995 mm to 10.414 mm, either the taper of section 1 had to be extended or a flare added to section 3. For the horn of Fig. 2(a), section 1 was extended. This again points out the difficulty of working with an over-simplified analysis.

Figures 5 and 6 show the far-field patterns of the prototype horn as measured on the near-field range. The estimated directivity of this horn from its aperture size, assuming uniform illumination of the aperture, is 11.99 dB at 32.3 GHz. This low directivity makes the horn more difficult to measure with a near-field range that uses a rectangular scan and, therefore, may not capture enough of the beam to provide accurate measurement of the antenna.

The E-plane patterns of Fig. 5 represent a pattern in the y–z plane of Fig. 3 for a y-polarized excitation. Since there is no explicit y-variation excited by the TE01 input, a reasonable match to the theory of uniform aperture excitation is expected. The theoretical patterns shown in Fig. 5 are calculated for aperture dimensions of 10.414 mm and 12.42 mm. The former represents the dimension of the aperture

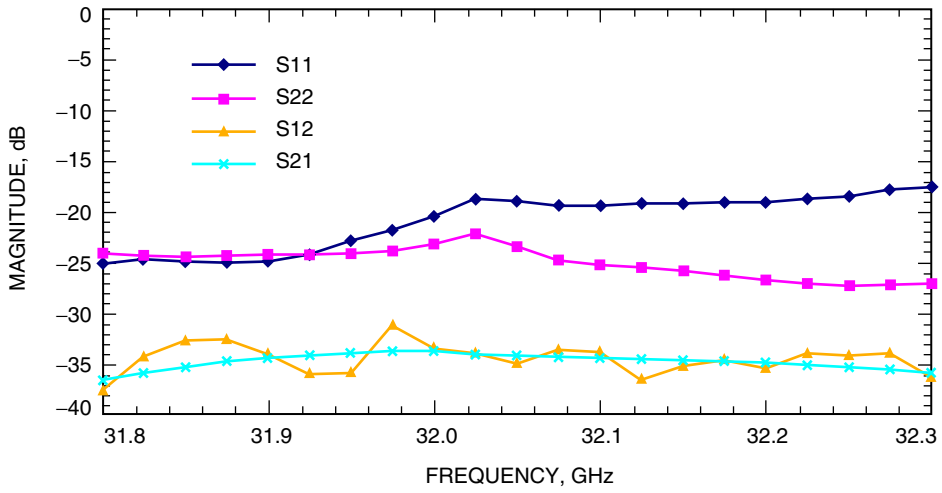

Fig. 3. Scattering parameters for the horn of Fig. 2(a) radiating into free space.

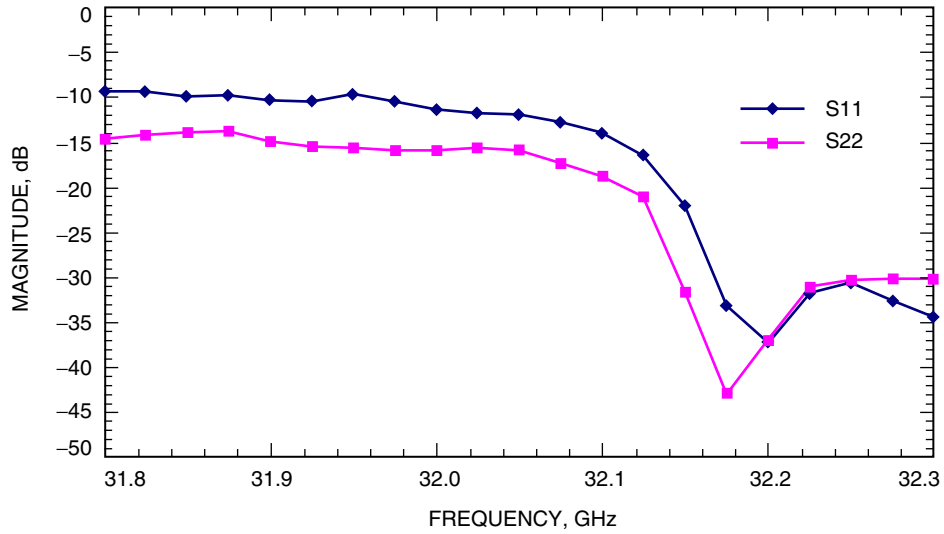

Fig. 4. Scattering parameters for the horn of Fig. 2(a) with the 10.414-mm aperture shorted.

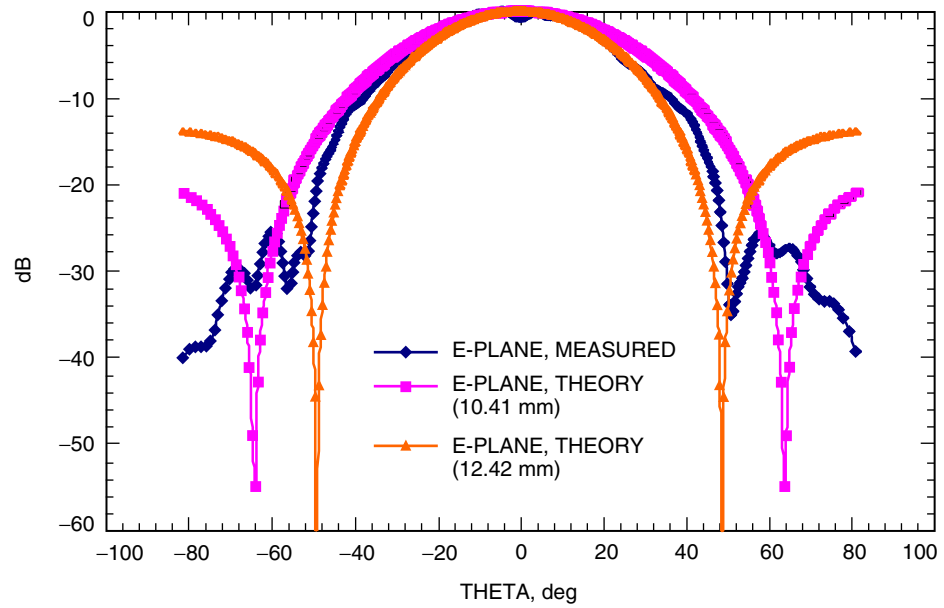

Fig. 5. Far-field pattern, E-plane, for the horn of Fig. 2(a) at 32.05 GHz.

inside the corrugations, while the latter includes half the corrugation depth on either side. For a uniform aperture, the first side lobe is 13.2 dB down from the main beam, provided the aperture is large enough so that $a \geq 1.44\lambda$. Figure 5 shows that the small size of this horn aperture begins to approach this limit for $a = 12.42$ mm.

In contrast to the E-plane patterns, the variation in Fig. 6 from the theory of uniform aperture excitation is a measure of the uniformity of the fields created by the hard boundary condition. In evaluation of these far-field measurements, we note the low directivity of this horn and that the horn was not designed to radiate into free space. The uniform modes as taken from the design parameters given later in Table 1 are for an infinitely long waveguide. Therefore, the reflection from the aperture radiating into space has not been accounted for in the design.

Figure 6 again shows plots for two uniform-aperture sizes, inside the corrugations and including half the corrugation depth. The larger aperture size allows for some radiation from the dielectric-filled corrugations and matches more closely to the measured patterns. As mentioned previously, the fields are finite in the corrugations. (The field taper in the corrugations is given in Table 1 in the next section.)

Figure 7 shows the H-plane pattern of the horn for a frequency of 32.3 GHz. As shown in Fig. 4, this is an area where the horn loss increases, possibly due to excitation of higher-order modes. There is a noticeable rise in the side lobe level of the measured pattern at this frequency (shown in Fig. 7).

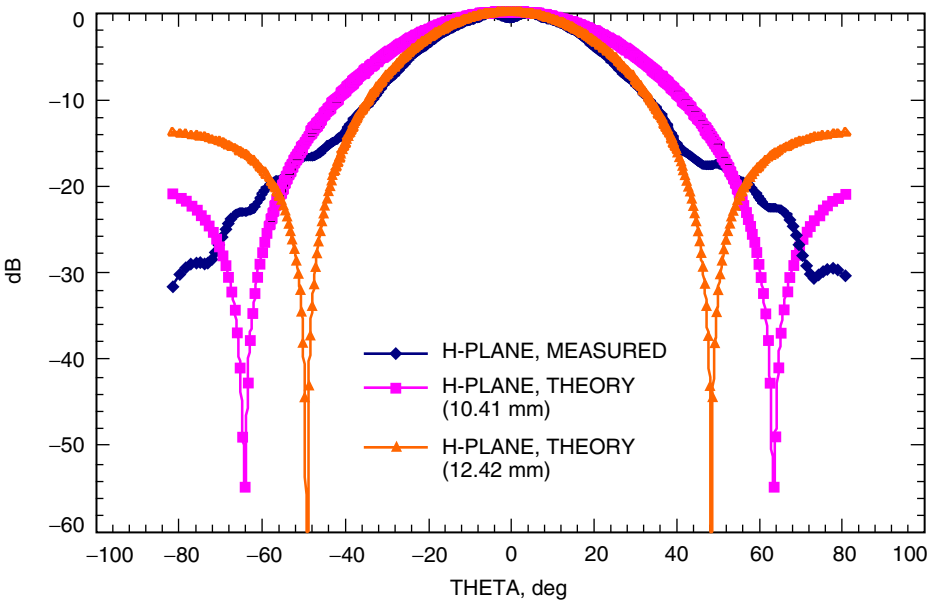

Fig. 6. Far-field pattern, H-plane, for the horn of Fig. 2(a) at 32.05 GHz.

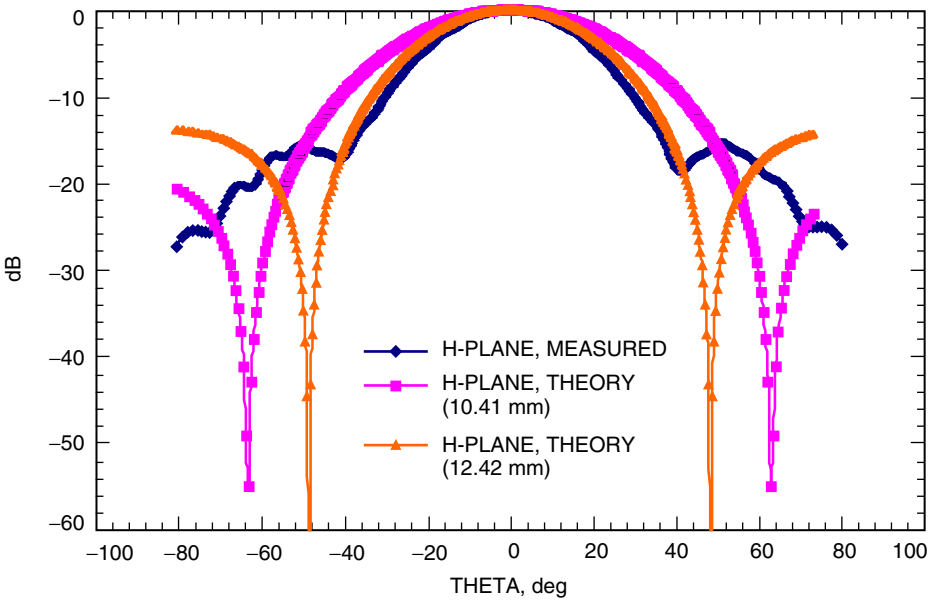

Fig. 7. Far-field pattern, H-plane, for the horn of Fig. 2(a) at 32.3 GHz.

The original intent of the near-field measurements was to get a far-field pattern, from which the near-field pattern could be derived, to get a representation of the aperture fields. Unfortunately, this feature of the near-field range does not work. In lieu of these measurements, raw data were used to view the aperture distribution as the near-field probe swept across the aperture of the horn 3.81 cm away. These curves are shown in Figs. 8 and 9. Figure 8 shows a variation of less than 1 dB in field magnitude over the aperture extents at the distance of 3.81 cm. Figure 9 shows an approximately 10-deg phase variation. Note that these patterns are taken in the far-field region, which for this small horn at 32.3 GHz is

$$\frac{2D^2}{\lambda} = 2.34 \text{ cm } (0.92 \text{ in.}) \tag{1}$$

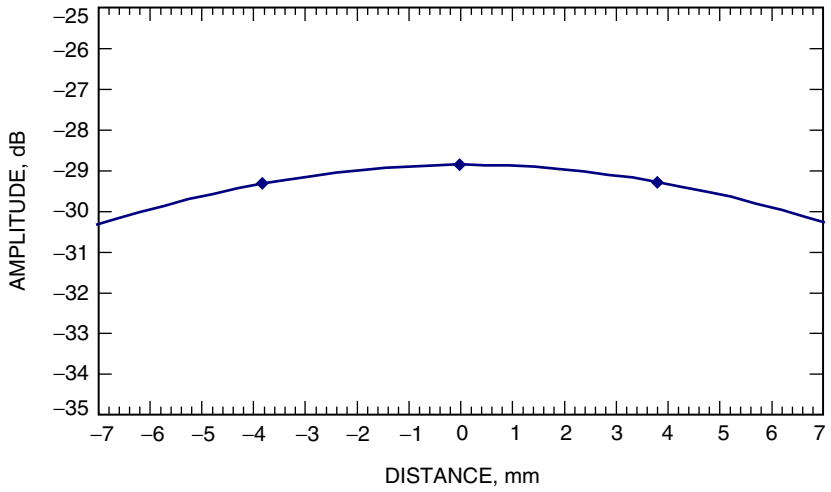

Fig. 8. Magnitude of the far-field pattern, H-plane, 32.05 GHz, for the horn of Fig. 2(a) at a distance of 3.81 cm. The distance represents the x-axis measurement of the probe.

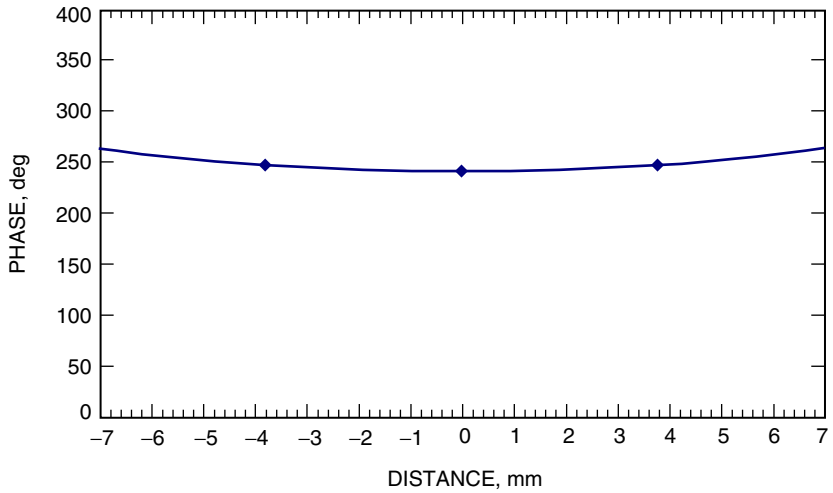

Fig. 9. Phase of the far-field pattern, H-plane, 32.05 GHz, for the horn of Fig. 2(a) at a distance of 3.81 cm. The distance represents the x-axis measurement of the probe.

III. Single-Mode Analysis and Design of a Hard Horn

In this section, the simplified analysis of Kildal [5] is used to design the hard horn of Fig. 2(a) with the axial cross section shown in Fig. 1. Using this simplified analysis, the horn was built and measured. This process provided information on the limitations involved in this design procedure. Consider the corrugated hard-horn cross section as shown in Fig. 10. Following the derivation of Kildal [5], the desired y-polarized mode is solved by considering a field representation in the guide region S_g, of dimensions a and b, and a field representation internal to a corrugated region S_c, which are equated via their common boundary conditions.

Consider first the field representation in the dielectric region of the form

$$E_y = -KA \sin\left[K\left(x - \frac{a}{2} - d\right)\right], \quad \frac{a}{2} < |x| < \frac{a}{2} + d \tag{2}$$

where $K = \sqrt{k_d^2 - k_z^2}$, with $k_d^2 = \omega^2 \mu\varepsilon$ and $k_z^2 = k_o^2 - k_x^2 + k_y^2$, and a dominant y-polarized wave is assumed. Here the values of k_x and k_y are the eigenvalues for the x- and y-directions, respectively. The corresponding tangential magnetic field component then is

$$H_z = \frac{K^2 A}{j\omega\mu} \cos\left[K\left(x - \frac{a}{2} - d\right)\right], \quad \frac{a}{2} < |x| < \frac{a}{2} + d \tag{3}$$

where $e^{-\Gamma z}$ dependence is assumed.

In order to enforce the boundary condition at $x = a/2$, it is useful to define the wall admittance:

$$\frac{H_z}{E_y} = \frac{-K \cot(-Kd)}{j\omega\mu} \tag{4}$$

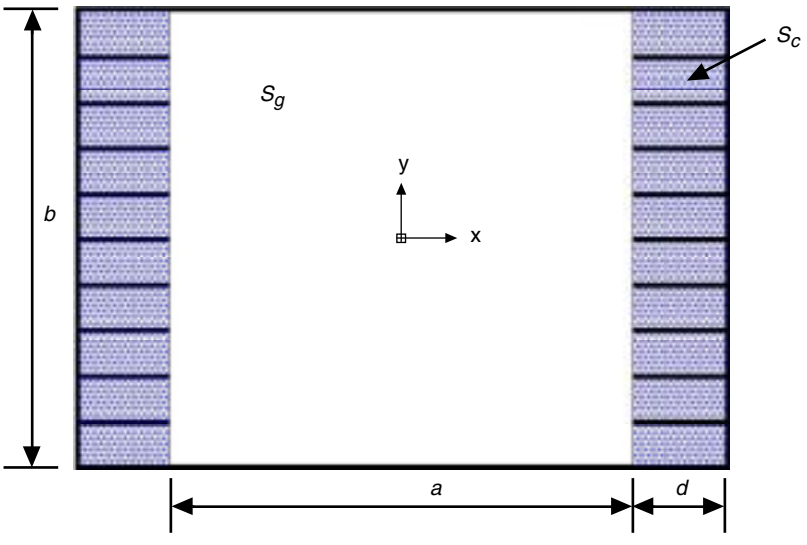

Fig. 10. Corrugated hard horn cross section.

The solution in the guide region S_g for the desired mode is then of the form

$$E_y = k_x \cos(k_x x), \quad |x| < \frac{a}{2} \tag{5}$$

Thus, this solution is immediately limited to a cosine distribution with no y-variation and to a single set of mode numbers, k_x. In understanding the development of the more general and complete set to be derived later, it is useful to follow the notation of Dybdal [7] for the guide region S_g. In this more general notation, it is realized that the y-polarized electric field may have y-variation as well as x-variation:

$$E_y = g_1(x)\, g_2(y), \quad |x| < \frac{a}{2} \tag{6}$$

which, by equating with Eq. (5), yields

$$\left.\begin{aligned} g_1(x) &= k_x \cos(k_x x) \\ g_2(y) &= 1 \end{aligned}\right\} \tag{7}$$

Following through with this, it also is seen that functional variation in x for the x-component of the E-field can be expressed as

$$f_1(x) = -K_2 k_x^2 \sin(k_x x) \tag{8}$$

which by Eq. (20) of Dybdal [7] shows that it is reasonable to assume that the magnetic field is of the form

$$H_z = \frac{k_x^2}{j\omega\mu} \sin(k_x x), \quad |x| < \frac{a}{2} \tag{9}$$

Thus, it becomes clear that the mode for which the solution is desired is a TE mode, or H mode. For later reference, it is noted that $f_1(x)$ has a sine representation.

In the same manner as before, wall admittance is defined at $x = a/2$:

$$\frac{H_z}{E_y} = \frac{k_x \tan\left(k_x \frac{a}{2}\right)}{j\omega\mu} \tag{10}$$

Enforcing the boundary condition at $x = a/2$, as defined in Eqs. (4) and (10), leads to the characteristic equation for the k_x:

$$k_x \tan\left(k_x \frac{a}{2}\right) = K \cot(Kd) \tag{11}$$

This equation can be solved for the TEM-like case if a solution can be found for which k_x is small. Such a solution is

$$d = \frac{\lambda}{4\sqrt{\varepsilon_r - 1}} \tag{12}$$

For $\varepsilon_r = 2.2$, the design parameters are given in Table 1 and are shown in Fig. 4 for the solution of Eq. (12).

Starting with these design parameters, a solution is sought for a corrugation depth sufficiently away from the possible surface wave at the highest frequency of interest. For this application, the band of interest is 31.8 GHz to 32.3 GHz. Figure 11 shows the dimensions for the corrugations and fins of the horn that was built and tested, as shown in Fig. 2(a). Note that the solution process gives no guidance for the thickness of the fin separating the corrugations. In keeping with a desire to have 10 corrugations per wavelength, where at least two corrugations per wavelength are needed [8], a fin thickness of 0.15 mm was chosen for this application. This fin thickness was based on the reasonably smallest fin that could be machined into aluminum using wire electrical discharge machining (EDM).

Table 1. Design parameters for the horn shown in Fig. 2(a).

Corrugation depth, mm	$k_x a/\pi$ at 32.3 GHz	Edge taper, dB	Guide wavelength λ_g, mm
0.0	1	$-\infty$	10.48
0.5	0.905	−16.5	10.20
1.0	0.8	−10.2	9.995
1.5	0.65	−5.6	9.73
2.0	0.32	−1.14	9.38
2.1	0.13	−0.18	9.297
2.118	0.0	0.0	9.28
2.152	Surface wave	—	—

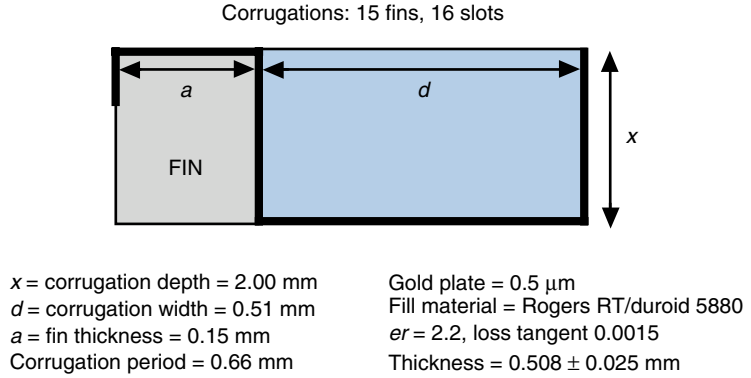

Fig. 11. Corrugation dimensions and fill-material description for the horn of Fig. 2(a).

IV. Analytical Development of a Complete Modal Set

An analytical model of a hard guide was developed from the separation-of-variables solution of the three-dimensional vector wave equation expressed in Cartesian coordinates. Modes corresponding to the standard TE (H) and transverse magnetic (TM) (E) modes were derived for the hard guide based on wall impedance relations presented by Dybdal [7]. The derived modes were realized using the modal analysis method reported by D. Hoppe of JPL [9]. A complete derivation is given in detail in the Appendix of this article. A brief summary follows here.

We begin with the definition of the wave impedances at the guide wall, defined in Fig. 10 as the region in the center bounded on top and bottom by PEC walls and on the sides by the dielectric-filled corrugations, denoted S_g:

$$\left.\begin{aligned} Z_1 &= \pm\frac{E_x}{H_z}\bigg|_{y=\mp(b/2)} \\ Z_2 &= \mp\frac{E_z}{H_x}\bigg|_{y=\mp(b/2)} \\ Z_3 &= \pm\frac{E_z}{H_y}\bigg|_{x=\mp(a/2)} \\ Z_4 &= \mp\frac{E_y}{H_z}\bigg|_{x=\mp(a/2)} \end{aligned}\right\} \tag{13}$$

We express the electric field traveling in the positive z-direction in Cartesian coordinates in a separable form as

$$\overline{E} = \left[\hat{x}\cdot f_1(x)f_2(y) + \hat{y}\cdot g_1(x)g_2(y) + \hat{z}\cdot h_1(x)h_2(y)\right]e^{-jk_z z} \tag{14}$$

We find the magnetic field expressed in corresponding notation by applying Maxwell's equations to be

$$\overline{H} = \begin{bmatrix} \hat{x}\cdot\left(h_1(x)h_2'(y) + jk_z g_1(x)g_2(y)\right) \\ -\hat{y}\cdot\left(h_1'(y)h_2(x) + jk_z f_1(x)f_2(y)\right) \\ +\hat{z}\cdot\left(g_1'(y)g_2(x) - f_1(x)f_2'(y)\right) \end{bmatrix} \frac{e^{-jk_z z}}{-j\omega\mu} \tag{15}$$

In Eqs. (14) and (15), k_z is the eigenvalue (propagation constant) related to the z-direction. It is defined by the separation equation in terms of the wave constant in the medium filling the guide and of the eigenvalues for the x- and y-directions as

$$k_x^2 + k_y^2 + k_z^2 = k^2 \tag{16}$$

Equation (16) follows from the wave equation for a source-free medium, where $k^2 = \omega^2\mu\varepsilon$, which is expressed in Cartesian coordinates as

$$\left[\frac{\partial^2}{\partial x^2}+\frac{\partial^2}{\partial y^2}+\left(k^2-k_z^2\right)\right]\cdot\left\{\begin{array}{c}E_x\\E_y\\E_z\end{array}\right\}=0 \tag{17}$$

When we apply Eqs. (14) and (15) in Eq. (13), it becomes convenient to define some constants in order to express the impedance relations in a manageable form. These constants are expressed in keeping with the notation of Dybdal as follows:

$$\left.\begin{aligned}Z_1&=\frac{f_1(x)f_2(y)}{g_1'(x)g_2(y)-f_1(x)f_2'(y)}\\Z_2&=\frac{-h_1(x)h_2(y)}{h_1(x)h_2'(y)+\Gamma g_1(x)g_2(y)}\\Z_3&=\frac{h_1(x)h_2(y)}{\Gamma f_1(x)f_2(y)-h_1'(x)h_2}\\Z_4&=\frac{-g_1(x)g_2(y)}{g_1'(x)g_2(y)-f_1(x)f_2'(y)}\end{aligned}\right\} \tag{18}$$

In Eq. (18), $\Gamma = jk_z$. Because the impedance at a given wall is a fixed value, which is independent of x and y, the relations of Eq. (18) require the following relationships between the components of the electric field:

$$\left.\begin{aligned}g_1'(x)g_2(y)&=L_1f_1(x)f_2'(y)\\h_1(x)h_2'(x)&=-\Gamma L_2g_1(x)g_2(y)\\h_1'(x)h_2(y)&=\Gamma L_3f_1(x)f_2(y)\end{aligned}\right\} \tag{19}$$

Application of standard separation-of-variables techniques yields the proportionality constants:

$$\left.\begin{aligned}h_1(x)&=K_1g_1(x)\\h_2(y)&=K_3f_2(y)\\f_1(x)&=K_2g_1'(x)\\g_2(y)&=K_4f_2'(y)\end{aligned}\right\} \tag{20}$$

Applying Eq. (20) in Eq. (19), we can define

$$\left.\begin{aligned} \delta &= \frac{K_4}{K_2} \\ \gamma &= \frac{\Gamma K_2}{K_1 K_3} \end{aligned}\right\} \tag{21}$$

Using Eqs. (19) through (21) and the condition of separability that

$$\left.\begin{aligned} f_1''(x) &= -k_x^2 f_1(x) \\ f_2''(y) &= -k_y^2 f_2(y) \end{aligned}\right\} \tag{22}$$

we can rewrite the expressions for the electric and magnetic fields in terms of the functional variation of E_x and the constants δ and γ as

$$\left.\begin{aligned} E_x &= f_1(x) f_2(y) & H_x &= \frac{-j}{\omega\mu} \frac{\Gamma f_1'(x) f_2'(y)}{k_x^2} \left(\frac{1}{\gamma} + \delta\right) \\ E_y &= -\frac{\delta}{k_x^2} f_1'(x) f_2'(y) & H_y &= \frac{-j}{\omega\mu} \Gamma f_1(x) f_2(y) \left(\frac{1}{\gamma} + 1\right) \\ E_z &= -\frac{\Gamma}{k_x^2 \gamma} f_1'(x) f_2(y) & H_z &= \frac{j}{\omega\mu} f_1(x) f_2'(y)(\delta - 1) \end{aligned}\right\} \tag{23}$$

From Eq. (23), we can see that $\delta = 1$ corresponds to the TM modes and $\delta = \infty$ corresponds to the TE modes. For the assumed isotropic, source-free medium filling the guide in the region defined by S_g in Fig. 10, $\nabla \cdot \bar{E} = 0$, which when applied to Eq. (23) yields

$$1 + \delta \left(\frac{k_y}{k_x}\right)^2 + \frac{1}{\gamma} \left(\frac{\Gamma}{k_x}\right)^2 = 0 \tag{24}$$

Substitution of Eq. (23) into Eq. (13) yields the general functional expressions for the impedance at the walls of a waveguide of rectangular geometry with arbitrary impedance boundary conditions:

$$\left.\begin{aligned} Z_1 &= \mp \frac{j\omega\mu}{(\delta - 1)} \frac{f_2(y)}{f_2'(y)}\bigg|_{y=\mp(b/2)} \\ Z_2 &= \pm \frac{j\omega\mu}{(1 + \gamma\delta)} \frac{f_2(y)}{f_2'(y)}\bigg|_{y=\mp(b/2)} \\ Z_3 &= \mp \frac{j\omega\mu}{k_x^2(1 + \gamma)} \frac{f_1'(x)}{f_1(x)}\bigg|_{x=\mp(a/2)} \\ Z_4 &= \mp \frac{j\omega\mu}{k_x^2} \left(\frac{\delta}{\delta - 1}\right) \frac{f_1'(x)}{f_1(x)}\bigg|_{x=\mp(a/2)} \end{aligned}\right\} \tag{25}$$

The impedance boundary conditions of Eq. (25) result in the "impedance compatibility relations":

$$\left.\begin{aligned} Z_1(\delta-1) &= -Z_2(\gamma\delta+1) \\ Z_3(1+\gamma)\delta &= Z_4(\delta-1) \end{aligned}\right\} \tag{26}$$

These conditions must be satisfied in order for the fields to be a solution of Maxwell's equations and for the wave equation to be properly separated. Written in matrix form, Eq. (26) becomes

$$\begin{bmatrix} Z_1 - Z_2 & -Z_2 \\ Z_4 & Z_3 \end{bmatrix} \begin{Bmatrix} 1/\delta \\ \gamma \end{Bmatrix} = \begin{Bmatrix} Z_1 \\ Z_4 - Z_3 \end{Bmatrix} \tag{27}$$

Solving Eq. (27) for δ and γ using Cramer's rule yields $\delta = 1$ and $\gamma = -1$. However, inserting these values into Eq. (24) gives the DC solution. The only conclusion that can be reached is that δ and γ are not independent, so that the determinant of $\mathbf{A}$ in Eq. (27) must be zero, which yields

$$\det(A) = Z_1 Z_3 - Z_2 Z_3 + Z_2 Z_4 = 0 \tag{28}$$

Since $Z_1 = Z_2 = 0$ in a linearly polarized horn, Eqs. (27) and (28) are satisfied.

At this point, we depart from Dybdal's work and move on to practical implementation of a complete mode set including both TM and TE modes. As reported [1,7,12], the standard TM modes for a rectangular waveguide with which we are all familiar satisfy the hard boundary condition and, as a result, propagate unperturbed in a hard guide, and so the proof will not be repeated here. Contrary to Dybdal, and as reported previously [1,12], TE modes also can exist, albeit in a modified form. These modified modes and the standard TM modes combine to form the complete hard guide mode set. Here the complete set is broken down into TM and TE half sets and presented in terms of four possible combinations of sine–cosine function products.

In the most general form, the separation-of-variables solution to the Cartesian wave equation for rectangular structures contains contributions from both TE and TM modes, described as the summation of weighted products of sine and cosine varying field components. The boundary conditions of the PEC wall guide dictate that the weights of three of the four possible sine–cosine products evaluate to zero. For the hard guide, this is not necessarily true, and since the actual impedance of the wall is unknown, all four components must be retained in the expression of the electric and magnetic fields.

TM Modes:

Cosine–Cosine:

$$f_1(x) = A_{cc} k_{xcc} \cos(k_{xcc} x) \qquad f_2(y) = \cos(k_{ycc} y) \tag{29a}$$

Sine–Cosine:

$$f_1(x) = A_{sc} k_{xsc} \sin(k_{xsc} x) \qquad f_2(y) = \cos(k_{ysc} y) \tag{29b}$$

Sine–Sine:

$$f_1(x) = A_{ss}k_{xss}\sin(k_{xss}x) \qquad f_2(y) = \sin(k_{yss}y) \tag{29c}$$

Cosine–Sine:

$$f_1(x) = A_{cs}k_{xcs}\cos(k_{xcs}x) \qquad f_2(y) = \sin(k_{ycs}y) \tag{29d}$$

TE Modes:

Cosine–Cosine:

$$f_1(x) = A_{cc}k_{ycc}\cos(k_{xcc}x) \qquad f_2(y) = \cos(k_{ycc}y) \tag{29e}$$

Sine–Cosine:

$$f_1(x) = A_{sc}k_{ysc}\sin(k_{xsc}x) \qquad f_2(y) = \cos(k_{ysc}y) \tag{29f}$$

Sine–Sine:

$$f_1(x) = A_{ss}k_{yss}\sin(k_{xss}x) \qquad f_2(y) = \sin(k_{yss}y) \tag{29g}$$

Cosine–Sine:

$$f_1(x) = A_{cs}k_{ycs}\cos(k_{xcs}x) \qquad f_2(y) = \sin(k_{ycs}y) \tag{29h}$$

There is a set of four products for both TM and TE modes. For TM modes, each product in Eqs. (29a) through (29d) represents an even–odd portion of the mode which when combined forms the complete standard mode set. A similar situation exists for the TE modes, although the partitioning of contributors is not as clear. The total field can be expressed as the summation

$$\bar{E}_{tot} = \sum_{E} \bar{E}_{cc} + \bar{E}_{sc} + \bar{E}_{ss} + \bar{E}_{cs} + \sum_{H} \bar{E}_{cc} + \bar{E}_{sc} + \bar{E}_{ss} + \bar{E}_{cs} \tag{30}$$

To avoid redundancy, we will concern ourselves here only with the cosine–cosine product because the development for all four is very similar. Applying Eq. (29) in Eq. (25), the impedance relations can be rewritten for the cosine–cosine case as

$$Z_1 = \left.\frac{\pm j\omega\mu\cot(k_y y)}{(\delta-1)k_y}\right|_{y=\mp(b/2)} \Rightarrow \frac{\cot(k_y b/2)}{(\delta-1)} = \frac{Z_1 k_y}{-j\omega\mu} \tag{31a}$$

$$Z_2 = \left.\frac{\mp j\omega\mu\cot(k_y y)}{(1+\delta\gamma)k_y}\right|_{y=\mp(b/2)} \Rightarrow \frac{\cot(k_y b/2)}{(1+\delta\gamma)} = \frac{Z_2 k_y}{j\omega\mu} \tag{31b}$$

$$Z_3 = \left.\frac{\pm j\omega\mu \tan(k_x x)}{(1+\gamma)k_x}\right|_{x=\mp(a/2)} \Rightarrow \frac{\tan(k_x a/2)}{(1+\gamma)} = \frac{Z_3 k_x}{-j\omega\mu} \tag{31c}$$

$$Z_4 = \left.\frac{\pm j\omega\mu\delta \tan(k_x x)}{(\delta-1)k_x}\right|_{x=\mp(a/2)} \Rightarrow \frac{\delta\tan(k_x a/2)}{(\delta-1)} = \frac{Z_4 k_x}{-j\omega\mu} \tag{31d}$$

Characteristic equations are found by applying the boundary conditions to Eq. (31).

TM Mode:

$$\delta = 1 \Rightarrow \cot\left(\frac{k_y b}{2}\right) = 0 \rightarrow k_y = \left.\frac{(2n-1)\pi}{b}\right|_{\substack{n\neq 0 \\ n=1,2,3\cdots}} \tag{32a}$$

$$\delta = 1 \Rightarrow \frac{j\omega\mu}{k_o^2}\left(k_x^2 + k_y^2\right)\cot\left(\frac{k_y b}{2}\right) = Z_2 k_y \tag{32b}$$

$$\delta = 1 \Rightarrow \frac{-j\omega\mu}{k_o^2}\left(k_x^2 + k_y^2\right)\tan\left(\frac{k_x a}{2}\right) = Z_3 k_x \tag{32c}$$

$$\delta = 1 \Rightarrow \tan\left(\frac{k_x a}{2}\right) = 0 \rightarrow k_x = \left.\frac{2m\pi}{a}\right|_{m=0,1,2\cdots} \tag{32d}$$

TE Mode:

$$\gamma = \infty \Rightarrow j\omega\mu k_y \cot\left(\frac{k_y b}{2}\right) = Z_1\left(k_x^2 + k_y^2\right) \tag{33a}$$

$$\gamma = \infty \Rightarrow \frac{\cot\left(k_y b/2\right)}{(1+\delta\gamma)} \rightarrow 0 \tag{33b}$$

$$\gamma = \infty \Rightarrow \frac{\tan\left(k_x a/2\right)}{(1+\gamma)} \rightarrow 0 \tag{33c}$$

$$\gamma = \infty \Rightarrow -j\omega\mu k_x \tan\left(\frac{k_x a}{2}\right) = Z_4\left(k_x^2 + k_y^2\right) \tag{33d}$$

The propagation constants for the mode set are found by solving for the roots of the characteristic equations given in Eqs. (32) and (33). From the four products represented in Eq. (29), we find four unique characteristics equations, two for each transverse direction. Propagation constants for the TM modes found from the characteristic equations are seen to be those of the PEC TM mode solution. For the TE modes, we find the characteristic equation set to be the following:

Y-Direction:

$$j\omega\mu k_y \cot\left(\frac{k_y b}{2}\right) = Z_1\left(k_x^2 + k_y^2\right) \tag{34a}$$

$$-j\omega\mu k_y \tan\left(\frac{k_y b}{2}\right) = Z_1\left(k_x^2 + k_y^2\right) \tag{34b}$$

X-Direction:

$$-j\omega\mu k_x \tan\left(\frac{k_x a}{2}\right) = Z_4\left(k_x^2 + k_y^2\right) \tag{34c}$$

$$j\omega\mu k_x \cot\left(\frac{k_x a}{2}\right) = Z_4\left(k_x^2 + k_y^2\right) \tag{34d}$$

In order to determine the TE mode set for a given hard wall guide, it is necessary that the wall impedance be known. For the longitudinally corrugated horn, the wall impedance is approximated to be the input impedance of a short-circuited parallel plate waveguide of length equal to the corrugation depth. The impedance at the wall is found as the inverse of Eq. (4) for a corrugation depth d to be

$$Z_{\text{wall}} = \frac{j\omega\mu}{K}\tan(Kd) \tag{35}$$

The ideal hard boundary condition occurs in accordance with [8] when $Kd = \pi/2$, which forces the wall impedance to infinity. For the wall impedance given for a chosen corrugation depth, the characteristic equation can be solved for the propagation constants, k_x and k_y. For a linearly polarized guide, in which the values of k_y are known to be integer multiples of π/b, we thus can write the characteristic equations needed to find k_x by inserting Eq. (35) in Eqs. (34c) and (34d):

$$-k_x \tan\left(\frac{k_x a}{2}\right) = \frac{\left(k_x^2 + k_y^2\right)}{K}\tan(Kd) \tag{36a}$$

$$k_x \cot\left(\frac{k_x a}{2}\right) = \frac{\left(k_x^2 + k_y^2\right)}{K}\tan(Kd) \tag{36b}$$

Finding the roots of the complex transcendental equations, Eqs. (36a) and (36b), for all of the desired values of k_y will yield the complete mode set. Preliminary analysis of the behavior of the functions shows that the roots occur as purely real or purely imaginary values. The same analysis also indicates that Newton's method using the derivative may be employed to find the roots for any groove depth. Another candidate for solving the equations are a C++ version of Muller's method from Beckett and Hurt [10] in which deflation [11] is used until the error reaches the preset criteria, at which point the search continues without deflation until the criteria are again satisfied.

Once the characteristic equations are solved, we need only to compute the modal normalization constants, A_{xx}, which can be found by evaluating the Poynting vector over the guide cross section:

$$P_{AVE} = \frac{1}{2} \int_{-(b/2)}^{b/2} \int_{-(a/2)}^{a/2} \hat{z} \cdot \mathrm{Re}\left\{ \bar{E} \times \bar{H}^* \right\} dxdy = 1 \tag{37}$$

At this time, it is useful to define the wave impedances for the TE and TM modes:

$$Z_{TE} = \frac{j\omega\mu}{\Gamma} \tag{38a}$$

$$Z_{TM} = \frac{\Gamma}{j\omega\varepsilon} \tag{38b}$$

For the TM cosine–cosine modes, Eq. (37), normalized to 1-W average power,

$$A_{cc}^2 = Z_{TM} \left[\int_{-(b/2)}^{b/2} \int_{-(a/2)}^{a/2} k_x^2 \cos^2(k_x x) \cos^2(k_y y) + k_y^2 \sin^2(k_x x) \sin^2(k_y y)\, dxdy \right]^{-1} \tag{39}$$

For the TE cosine–cosine modes, Eq. (37), normalized to 1-W average power,

$$A_{cc}^2 = Z_{TE} \left[\int_{-(b/2)}^{b/2} \int_{-(a/2)}^{a/2} k_y^2 \cos^2(k_x x) \cos^2(k_y y) + k_x^2 \sin^2(k_x x) \sin^2(k_y y)\, dxdy \right]^{-1} \tag{40}$$

Using these and similar expressions for each of the four products for both the TE and TM mode sets in Eq. (29) will provide the complete power-normalized field expressions for each mode. These normalized field expressions then can be applied in the manner presented in [4] to generate the equations for the scattering matrix for a hard boundary wall waveguide.

V. Conclusions

Work continues on the development of the hard horn in multiple areas. The modal solution is still being pursued. In addition to the modal solution, a finite element method (FEM) eigen-mode solver has been under development for some time, and we expect to produce complete field simulations for hard boundary waveguides in the very near future. Results from the FEM and the modal solution will be compared with each other and with the measured results of the prototype horn. In addition to the analytical work, a second prototype has been fabricated, and analysis is ongoing. Hard boundary waveguide pieces also are slated for fabrication to investigate insertion loss and bandwidth characteristics of hard guides. The measured results of the second hard horn and those from the hard guides will be compared with predicted results from the FEM and modal solutions and, to the extent possible, with simulations using Ansoft's High Frequency Structure Simulator.

Acknowledgments

The authors would like to thank Raul M. Perez for his measurement assistance in testing the hard horn and Harry F. Reilly, Jr. for his assistance in fabricating the horn.

References

[1] E. Lier and P.-S. Kildal, "Soft and Hard Horn Antennas," *IEEE Trans. Antennas Propagation*, vol. 36, no. 8, pp. 1152–1157, August 1988.

[2] J. W. Mink, "Quasi-Optical Power Combining of Solid-State Millimeter-Wave Sources," *IEEE Trans. Microwave Theory Tech.*, vol. MTT-34, no. 2, pp. 273–279, February 1986.

[3] K. Chang and C. Sun, "Millimeter-Wave Power-Combining Techniques," *IEEE Trans. Microwave Theory Tech.*, vol. MTT-31, no. 2, pp. 91–107, February 1983.

[4] J. Harvey, E. R. Brown, D. B. Rutledge, and R. A. York, "Spatial Power Combining for High Power Transmitters," *IEEE Microwave Magazine*, vol. 1, no. 4, pp. 48–59, December 2000.

[5] P.-S. Kildal, "Bandwidth of a Square Hard Horn," *IEE Proceedings*, vol. 135, pt. H, no. 4, pp. 275–278, August 1988.

[6] S. P. Skobelev and P. S. Kildal, "Analysis of a Hard Corrugated Conical Horn by Using the Method of Generalised Scattering Matrices," Eleventh International Conference on Antennas and Propagation, IEE Conference Publication no. 480, vol. 2, pp. 696–700, April 2001.

[7] R. B. Dybdal, L. Peters, Jr., and W. H. Peake, "Rectangular Waveguides with Impedance Walls," *IEEE Trans. Microwave Theory Tech.*, vol. MTT-19, no. 1, pp. 2–9, January 1971.

[8] P.-S. Kildal, "Definition of Artificially Soft and Hard Surfaces for Electromagnetic Waves," *Electronics Letters*, vol. 24, no. 3, pp. 168–170, February 1988.

[9] D. J. Hoppe, "Modal Analysis Applied to Circular, Rectangular, and Coaxial Waveguides," *The Telecommunications and Data Acquisition Progress Report 42-95, July–September 1988*, Jet Propulsion Laboratory, Pasadena, California, pp. 89–96, November 15, 1988.
http://tmo.jpl.nasa.gov/tmo/progress_report/42-95/95I.PDF

[10] R. Beckett and J. Hurt, *Numerical Calculations and Algorithms*, New York: McGraw-Hill, pp. 57–62, 1967.

[11] R. L. Johnston, *Numerical Methods, A Software Approach*, New York: John Wiley and Sons, pp. 173–177, 1982.

[12] P. R. McIsaac, "Comments on 'Rectangular Waveguides with Impedance Walls'," *IEEE Trans. Microwave Theory Tech.*, vol. 22, no. 11, pp. 972–973, November 1974.

Appendix
Standard TM Mode Proof

We write the summation of the x-component of the E-field for the complete TM mode as

$$E_x = A_{cc}k_{xcc}\cos\left(k_{xcc}x\right)\cos\left(k_{ycc}y\right) + A_{sc}k_{xsc}\sin\left(k_{xsc}x\right)\cos\left(k_{ysc}y\right)$$
$$+ A_{ss}k_{xss}\sin\left(k_{xss}x\right)\sin\left(k_{yss}y\right) + A_{cs}k_{xcs}\cos\left(k_{xss}x\right)\sin\left(k_{yss}y\right) \tag{A-1}$$

We break out the cosine–cosine and sine–cosine portions, insert propagation constants found from the separation-of-variables solution to the wave equation, and write

$$A_{cc}k_{xcc}\cos\left(k_{xcc}x\right)\cos\left(k_{ycc}y\right) = \left.A_{cc}\frac{m\pi}{a}\cos\left(\frac{m\pi}{a}x\right)\cos\left(\frac{n\pi}{b}y\right)\right|_{\substack{m=0,2,4\cdots \\ n=1,3,5\cdots}} \tag{A-2a}$$

$$A_{sc}k_{xsc}\sin\left(k_{xsc}x\right)\cos\left(k_{ysc}y\right) = \left.A_{sc}\frac{m\pi}{a}\sin\left(\frac{m\pi}{a}x\right)\cos\left(\frac{n\pi}{b}y\right)\right|_{\substack{m=1,3,5\cdots \\ n=1,3,5\cdots}} \tag{A-2b}$$

It can be shown that

$$A_{sc}^2 = A_{cc}^2 = 2Z_{TM}\left[\left(\frac{m\pi}{a}\right)^2 + \left(\frac{n\pi}{b}\right)^2\right]^{-1}\frac{\varepsilon_{om}\varepsilon_{on}}{ab}, \quad \varepsilon_{oq} = \begin{vmatrix} 0, & q = 0 \\ 2, & q > 0 \end{vmatrix} \tag{A-3}$$

Further simplification yields

$$A^2 = \frac{2Z_{TM}}{k_{mn}^2}\frac{\varepsilon_{om}\varepsilon_{on}}{ab}, \quad \varepsilon_{oq} = \begin{vmatrix} 0, & q = 0 \\ 2, & q > 0 \end{vmatrix} \tag{A-4}$$

Applying Eq. (A-4) and adding Eq. (A.2), we get

$$A\frac{m\pi}{a}\left[\left.\cos\left(\frac{m\pi}{a}x\right)\right|_{m=0,2,4\cdots} + \left.\sin\left(\frac{m\pi}{a}x\right)\right|_{m=1,3,5\cdots}\right]\left.\cos\left(\frac{n\pi}{b}x\right)\right|_{n=1,3,5} \tag{A-5}$$

We perform a substitution of variables to shift to a corner-centered guide where $x\prime = x + a/2$ and see that

$$\cos\left(\frac{m\pi}{a}x'\right) = \cos\left(\frac{m\pi}{a}x + \frac{m\pi}{2}\right) = \begin{vmatrix} (-1)^{(m+1)/2}\sin\left(\frac{m\pi}{a}x\right), & m = 1,3,5\cdots \\ (-1)^{m/2}\cos\left(\frac{m\pi}{a}x\right), & m = 0,2,4\cdots \end{vmatrix} \tag{A-6}$$

Absorb the sign into the normalization constants and apply Eq. (A-6) in Eq. (A-5):

$$A\frac{m\pi}{a}\cos\left(\frac{m\pi}{a}x+\frac{m\pi}{2}\right)\cos\left(\frac{n\pi}{b}y\right)\Big|_{n=1,3,5\cdots} \tag{A-7}$$

We break out the sine–sine and cosine–sine elements of Eq. (A-1), insert the known propagation constants, and write

$$A_{ss}k_{xss}\sin\left(k_{xss}x\right)\sin\left(k_{yss}y\right)=A_{ss}\frac{m\pi}{a}\sin\left(\frac{m\pi}{a}x\right)\sin\left(\frac{n\pi}{b}y\right)\Big|_{\substack{m=1,3,5\cdots\\ n=0,2,4\cdots}} \tag{A-8a}$$

$$A_{cs}k_{xcs}\cos\left(k_{xcs}x\right)\sin\left(k_{ycs}y\right)=A_{cs}\frac{m\pi}{a}\cos\left(\frac{m\pi}{a}x\right)\sin\left(\frac{n\pi}{b}y\right)\Big|_{\substack{m=0,2,4\cdots\\ n=0,2,4\cdots}} \tag{A-8b}$$

Applying the x-direction coordinate shift and adding Eq. (A-8) yields

$$A\frac{m\pi}{a}\cos\left(\frac{m\pi}{a}x+\frac{m\pi}{2}\right)\sin\left(\frac{n\pi}{b}y\right)\Big|_{n=0,2,4\cdots} \tag{A-9}$$

where the normalization constant A in Eq. (A-9) is the same as in Eq. (A-4). We add Eq. (A-9) and Eq. (A-7) to get

$$A\frac{m\pi}{a}\cos\left(\frac{m\pi}{a}x+\frac{m\pi}{2}\right)\left[\cos\left(\frac{n\pi}{b}y\right)\Big|_{n=1,3,5\cdots}+\sin\left(\frac{n\pi}{b}y\right)\Big|_{n=0,2,4\cdots}\right] \tag{A-10}$$

An axis shift where $y'=y+b/2$ gives the expression corresponding to Eq. (A-6) for the y-direction:

$$\sin\left(\frac{n\pi}{b}y'\right)=\sin\left(\frac{n\pi}{b}y+\frac{n\pi}{2}\right)=\begin{cases}(-1)^{(n-1)/2}\cos\left(\frac{n\pi}{b}y\right), & n=1,3,5\cdots\\ (-1)^{n/2}\sin\left(\frac{n\pi}{b}y\right), & n=0,2,4\cdots\end{cases} \tag{A-11}$$

Applying Eq. (A-11) in Eq. (A-10) yields the standard TM mode set that propagates in a rectangular waveguide with the coordinate system centered at the guide axis expressed as

$$A\frac{m\pi}{a}\cos\left(\frac{m\pi}{a}x+\frac{m\pi}{2}\right)\sin\left(\frac{n\pi}{b}y+\frac{n\pi}{2}\right) \tag{A-12}$$